Journal of
Ceramic Science
and Technology

J. Ceram. Sci. Tech., 02 [02] 75-88 (2011)
DOI: 10.4416/JCST2011-00003
available online at: http://www.ceramic-science.com

Methods of Quantification of the Internal Structures of Spray Granules

S. Höhn*, S. Eckhard, M. Fries, B. Matthey, M. Herrmann, A. Michaelis

Fraunhofer Institute for Ceramic Technologies and Systems, Winterbergstrasse 28, 01277 Dresden, Germany
received January 20, 2011; accepted February 28, 2011

Abstract

Granules for die pressing applications prepared by means of spray drying need to possess specific properties defined by the end-application. The internal structure of the granules is therefore an important quality-determining property because it influences both the processing properties of the loose granules and the defect distribution in the sintered ceramic part.

In this paper, an optimized, artifact-free, gentle and reproducible preparation method based on ion beam technology for exposing the internal granule structures is presented. Model Al_2O_3 granules are used to demonstrate the possibilities for imaging via high-resolution scanning electron microscopy and quantification of the granules in terms of porosity as well as particle and additive distribution.

Keywords: Granule, microstructure quantification, ion beam preparation, porosity, particle distance

I. Introduction

Handling, dosage and processing of ceramic powders with particle sizes in the submicron and nanometer ranges are only possible after an agglomeration step. One of the most common processes for preparing granules with tailored processing properties e.g. for die pressing is spray drying [1,2]. During the die pressing step the granules have to disintegrate completely into primary particles to form homogeneous structures of the green body. Besides other parameters, the internal granule structure has a strong influence on the deformation behavior of single granules and accordingly on the resulting compact quality. Defined granule structures suitable for the planned subsequent processing steps can be achieved through adaptation of the suspension properties and the spray parameters.

The development and characterization of the granule structure as a decisive property of ceramic spray granules has been described qualitatively in various publications in the last few decades. Correlations related to this are described by Soottitantawat *et al.* [2] and Walton *et al.* [3]. A direct relationship between granule structure and granule density, strength and resultant flow properties is reported. The development of various granule shapes over the course of drying is described by Masters [4]. The effect of particle mobility on the resultant internal granule structure is summarized by Walker *et al.* [5].

The granule structure has been characterized qualitatively by means of scanning electron microscopy (SEM) or subjective description. A complete, reproducible and objective method for internal granule structure characterization is lacking. Development of methods for gentle, reproducible preparation and image-analysis-based quantification of internal granule structures is hence the focus of this paper.

The relationship between suspension properties, granule structure, deformation properties, pressed green body structure and part strength is discussed in publications by Fries [6], Hotta *et al.* [7], Bertrand *et al.* [8,9], Lukasiewicz [10], Abe *et al.* [11] and Tsubaki *et al.* [12].

A quantitative method for structure characterization is a prerequisite for the formulation of scientifically founded correlations between process parameters, granule structure and product or processing properties.

II. Structural Characterization – State of the Art

The state of the art in the description of the granule and green body structures is the generation of optical microscope or SEM images of outer, fracture and cut surfaces. Usually, the results are evaluated subjectively, or a qualitative comparison of the particle size distributions and porosities of test specimens is performed [13,14]. Baklouti *et al.* [15] used SEM images to illustrate that the binder distribution can separate during spray drying. They detected a binder shell around the granule, with the shell thickness calculable on the basis of various simplifying assumptions. Tanaka *et al.* [16] observed clear differences in the behavior and distribution of the additives in a qualitative comparison of spray granules. They also determined the effect of the binder distribution on the deformation properties of the granules.

Mechanical preparation of granule sections is difficult. Information on the internal morphology can be obtained through mechanical section preparation with prior infiltration of the granules with organic embedding agents. However, this preparation method creates artifacts such

* Corresponding author: Soeren.Hoehn@ikts.fraunhofer.de

as pullouts of the loosely bound hard ceramic particles or smearing of the particles in the soft organic embedding materials. The organic additives in the granules are overpowered by the embedding matrix and thus cannot be visualized. Adequate characterization of the internal granule structure is hence often not possible.

Mercury porosimetry can be used for the evaluation of the microstructure's total porosity, average pore size and pore size distribution [17]. Interpretation of mercury porosity data is problematic, mainly owing to the problems in differentiating between the intragranular macroporosity and the porosity between the granule junctions. Quantitative analysis of the structure, the porosity and the solids distribution has not yet been achieved [3, 16, 18].

Another technique for characterization of porous structures is the immersion liquid technique (ILT) [19-24]. This method is based on the reduced light reflection at the interface between the powder particles and the surrounding medium in the presence of a liquid immersion medium. Uematsu *et al.* [19] and Kim *et al.* [20] showed that this method could be used to image internal granule regions at the resolution of an optical microscope.

In a publication by Zhang *et al.* [21], binder segregation at the surfaces of binder-enriched Al_2O_3 granules was described. Inhibition of the densification of Al_2O_3 particles owing to the high binder content was demonstrated with polarized light microscopy and ILT by Uematsu *et al.* [22]. The combination of ILT with IR microscopy for direct investigation of a pressed Al_2O_3 body was described by Uematsu *et al.* [23]. An increase in resolution was found to be achieved with the combination of a confocal laser scanning microscope [24]. The publications showed that with ILT, macropores and density gradients could be identified in granules. However, the method does not allow for quantitative statements to be made about particle relationships on the submicron and nanometer scales. Organic components and their distribution can only be shown if they are present in the specimen in sufficiently high amounts.

In recent times advances made in computer tomography (CT) have enabled new approaches for characterization of porous structures. The technique is used especially for macroscopic pore quantification [25-29]. The limiting factor here is the resolution of the computer tomograph. Farber *et al.* [26, 27] utilized computer tomography to examine the structure and porosity of pharmaceutical granules. Results of mercury porosimetry measurements performed for comparison purposes were in good agreement for the large pores. The small pores were not detected owing to the limited resolution of the CT. Resolutions of up to 1 µm could be achieved by Salvo *et al.* [28] using synchrotron radiation as a radiation source. A latest-generation high-performance computer tomograph was used as an aid for evaluating $CaCO_3$ granules in various conditions by Rahmanian *et al.* [29]. Granule structures could be reconstructed from the images at resolutions of less than 1 micron.

The state of the art presented shows that no methods currently exist for visualizing the granule structures at sufficient resolution for reproducible and objective image-analysis-based characterization. Imaging of structures on the submicron and nanometer scales is possible with the field emission scanning electron microscope (FESEM). The sample preparation technique must be adapted to the specific requirements of quantitative structural characterization and especially be suitable for reproducible and true-to-original imaging of solid particle, pore and binder distributions. Ion beam sputtering represents a gentle method of exposing the analysis surface of highly porous granule structures without introducing mechanical damage. The applicability of the technique for structural imaging of ceramic granules as well as green and sintered bodies has been published in earlier papers [6, 30-32].

III. Ion Beam Preparation

Sputtering of the surfaces of solids by ion beam irradiation was discovered back in the middle of the 19th century by Grove [33] and Plücker [34], when they observed a loss in cathode material in a gas discharge. Ion-assisted processes have been established in the semiconductor and electronics industry since the end of the 1980s. One application area is the structuring of surfaces for defined adjustment of geometries down to the nanometer scale [35, 36]. Ever finer structures on microelectronics components necessitated the development of new preparation methods for pinpointed exposure of components on the submicron and nanometer scales. The focused ion beam (FIB) technique could achieve this [37]. A major disadvantage of FIB is the size of the prepared surface. In a reasonable amount of time, only a few µm² can be prepared and this is usually insufficient for quantitative analysis.

For material removal over large surface areas for preparation of samples for transmission and scanning electron microscopy, ion sources with high current densities are required [38-40]. In this case, the broad ion beam technique (BIB) is referred to in the literature. It is possible to adjust the removal conditions specifically and to direct the ion beam either nearly field-free or selectively accelerated or decelerated by a specifically applied DC field onto the sample surface, leading selectively to etching or removal.

This method for low-defect preparation of sections through ceramics can hence serve as a basis for quantitative structural determination of granules and is used in this study for preparation.

IV. Materials and Methods

(1) Preparation of model granules

Five model granules were chosen for the investigation of different methods of quantification of internal granule structures.

Suspensions were prepared from Al_2O_3 raw material (Nabalox NO 713-10, Nabaltec, Germany) by means of milling and homogenization in an agitation ball mill. Citric acid was used as dispersant for samples 1 to 4 (0.25 wt%) during the homogenization process. No dispersant was used for sample 5.

Table 1: Suspension properties and spray-drying conditions.

	Units	Granule 1	Granule 2	Granule 3	Granule 4	Granule 5
Solid content	[wt%]	71.2	50.2	62.1	49.9	44.4
Viscosity	[Pas(240min^{-1})]	29	7.2	285.8	27.3	154.6
pH value	[-]	9.05	9.11	2.33	6.68	9.5
Density of suspension	[g/cm^3]	2.06	1.57	1.62	1.39	1.4
T (inlet)	[°C]	180	200	190	200	190
T (exit)	[°C]	85	85	84	86	90
Suspension mass flow	[kg/h]	5.80	4.60	4.84	4.45	2.42

For all samples, an organic binder (polyvinyl alcohol (PVA), 1 wt%) was added to improve stability during preparation, handling and processing steps. The suspension properties and accordingly the resulting granule structures were changed by variation of the solids content between 50.0 wt% and 71.2 wt%. A very high amount of citric acid was added for suspension 3, resulting in very high viscosities compared with those of the other suspensions and accordingly homogeneous internal structures. These variations resulted in different granule structures (Figs. 1, 8, 10 and 11).

Samples 4 and 5 were used for the preparation of two granules with different binder distributions within the granule microstructures. Comparably high amounts of binders were added (zinc stearate, 5 wt% for sample 4 and an acrylate binder "Duramax B1000", 7.5 wt% for sample 5). The aim of these tests was the visualization and quantification of different binder distributions.

All suspensions were characterized concerning solids content, pH value, viscosity and density. The results are summarized in Table 1.

The suspensions were spray dried under comparable conditions (Table 1) using a small-scale spray dryer (Mobil Minor, GEA Niro A/S, counter-current flow).

For all suspensions, a two-component nozzle with compressed air as the atomization gas was chosen. The drying gas was air in all cases and the nozzle pressure and the drying gas rate were kept as constant as possible (nozzle pressure between 0.2 bar and 0.3 bar, drying gas rate between 76 kg/h and 81 kg/h).

(2) Microstructural preparation using ion beams

The granule charges were prepared using the BAL-TEC RES101 ion beam etching system. Argon was used as the working gas. The system is equipped with two saddle field ion sources, which face each other and which have powers that can be varied over the range of approx. 1 W to 25 W. The sample rotates during the ion sputtering process. A Peltier element situated on the sample holder is available for temperature measurement and monitoring. A schematic diagram of the test setup is shown in Fig. 2.

For structural characterization, three test setups were used:

– For analysis of the organic components, the granules cannot be stabilized by means of resin infiltration because it cannot be distinguished from the embedding materials in the FESEM. Through gluing of the granules on the sample holder and then performing ion beam preparation in the equatorial plane, artifact-free structural imaging is possible (Fig. 3a). Ion beam preparation is a multistep process. The main material removal step is performed at a steep angle of incidence to the sample surface. This is followed by preparation steps at small, nearly parallel angles of incidence to the surface for the purposes of smoothing the analysis surface.

For quantitative micro- and macrostructural characterization in accordance with Section IV(4), embedding of the specimens in epoxy resin is useful, since it prevents the deeper specimen regions from being included in the grayscale detection process (cf. Fig. 4b).

– For sample preparation in the equatorial plane (Fig. 3b), the granules are applied as a fractionated monolayer on the sample holder, covered with epoxy resin and infiltrated under a vacuum. For reduction of the preparation time, the sample is ground with SiC P2500 grinding paper to approx. 10 µm from the equatorial plane. Through subsequent gentle removal using ion beams, the equatorial plane is approached, with the process being monitored in an optical microscope. The sample area thus obtained is free of artifacts such as pullouts and smeared particles.
– In the preparation of fractionated loose granules (Fig. 3c), the samples are infiltrated with epoxy resin and then also mechanically pre-ground. Subsequent ion removal is performed analogously to the preparation of granules in the equatorial plane.

(3) SEM and EDX analysis

For visualization of the prepared structures, the NVision 40 (Carl Zeiss SMT AG) FESEM was used. The device is a dual-beam microscope and also has an FIB unit, which was used for preparation with a comparable distribution of organic additives. An EDX detector (INCA Energy 350, OXFORD Instr.) was available for chemical analysis.

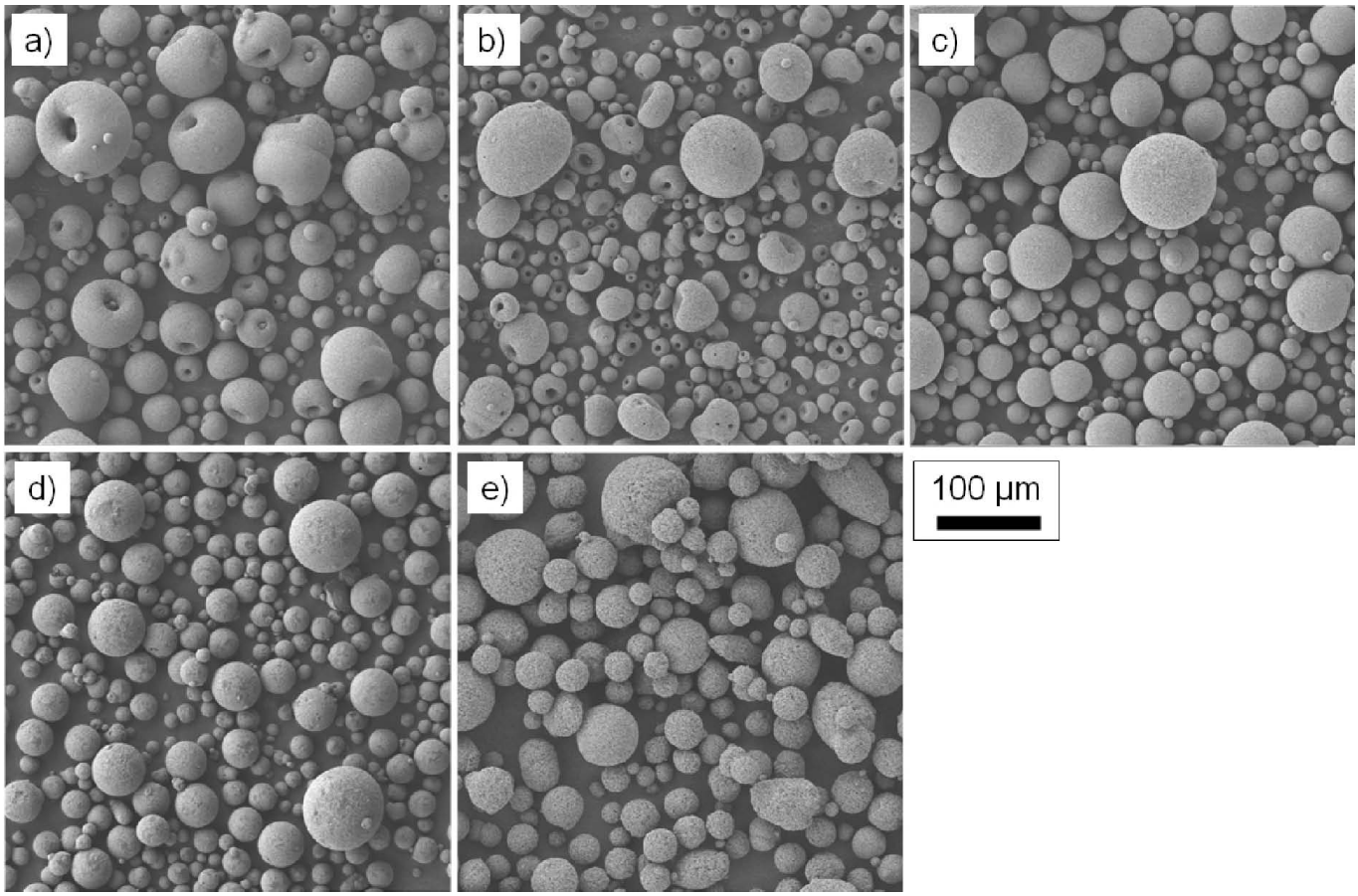

Fig. 1: Surface images: a) granule 1; b) granule 2; c) granule 3; d) granule 4; e) granule 5.

The macroscopic images were taken at a magnification of 150X with the QBSD detector (4-quadrant backscattered electron detector). At this magnification, it was possible to image the macroscopic pore surface appropriately without also detecting the microscopic pore fraction (Fig. 4a). Documentation of the microstructure was performed at a magnification of 20 000X (Fig. 4b) with the EsB detector (in-lens backscattered electron detector). For detection of the organic additive components, the SE detector (in-chamber detector) was used (Figs. 8 and 10-12).

(4) Quantitative structural analysis

For the investigations performed, the size fraction 45-63 µm was used for all granules; this fraction corresponded to the d_{50} value of the prepared model granules. Most of the structural parameters were determined using image analysis methods with the program AnalySIS FIVE (Olympus Soft Imaging Solutions GmbH).

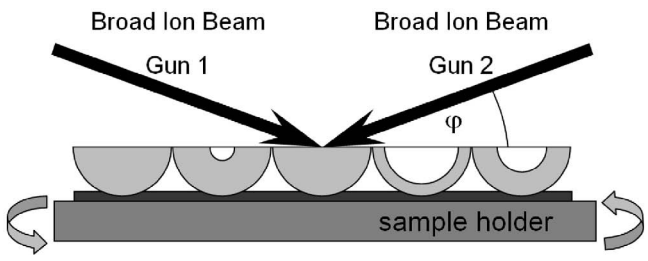

Fig. 2: Schematic diagram illustrating the test setup for the ion sputtering process.

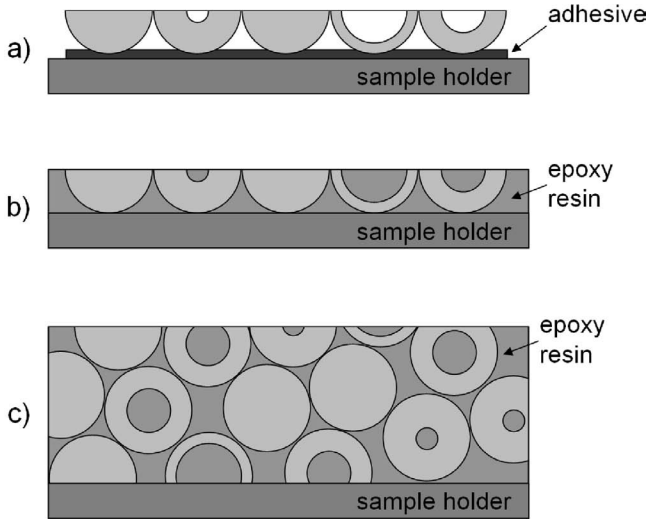

Fig. 3: Test setups for structural characterization: a) Scattered, fractionated monolayer for analysis of organic additive distribution, b) embedded granule fraction cut in equatorial plane, c) embedded scattered granule fraction.

For quantitative description of the internal granule structure, it is useful to differentiate between the macrostructure and the microstructure. Table 2 as well as Figs. 5 and 6 provide an overview of the main structural parameters used.

Table 2: Macroscopic and microscopic parameters for granule characterization.

	Parameter	Description
Macrostructural	P_{macro}	Macroscopic porosity (void in granule)
	P_{total}	Total porosity
	S	Average shell thickness of granule fraction
	H	Average ratio of hollow area to total surface area in equatorial plane
	M_{homo}, M_{hollow}, M_{inter}	Number-weighted fraction of solid ($H \leq 0.01$), hollow ($H \leq 0.1$) and intermediate granule forms ($0.01 < H \leq 0.1$)
Microstructural	P_{micro}	Interparticle porosity
	$D_{nn\text{-}surf}$	Primary particle surface spacing (indirect: pore size distribution)
	$d_{particle}$	Primary particle diameter/distribution

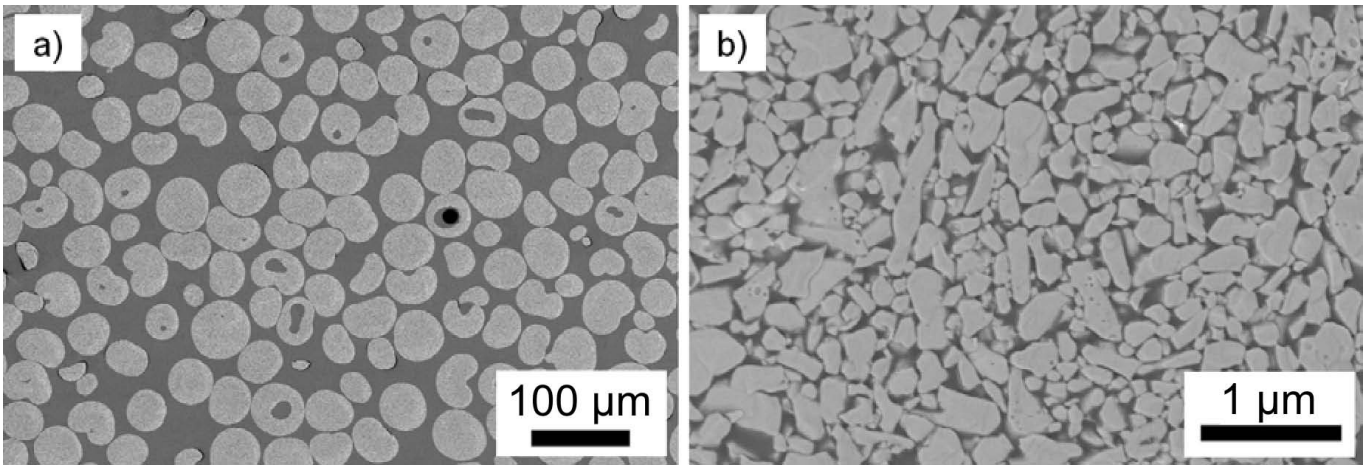

Fig. 4: Detectors and magnifications on FESEM for quantitative analysis of a) macrostructure: QBSD detector, 150X and b) microstructure: ESB detector, 20 000X.

Stereology can be used to determine the volume fraction from the surface area fraction by means of a planar polished section through loose granules (cross-sectional area – "cs"). This makes it possible to determine the macroscopic porosity P_{macro} from the area fraction of macropores $A_{void\text{-}cs}$ and the total area of the granules $A_{total\text{-}cs}$ using equation (1).

$$P_{macro} = \frac{\sum_{1}^{n} A_{void-cs}}{\sum_{1}^{n} A_{total-cs}} \cdot 100\ \% = \frac{\sum_{1}^{n} A_{void-cs}}{\sum_{1}^{n} A_{void-cs} + \sum_{1}^{n} A_{void-mi} + \sum_{1}^{n} A_{solid-mi}} \cdot 100\ \% \quad (1)$$

A cut through the equatorial plane ("e") is necessary for precise determination of the distribution of macropores in the granules. The images produced can be used for determination of the shell thickness *S* of the hollow granules. In addition, the parameter *H* is defined; this parameter is determined on granules cut in the middle as the quotient of the sum of all macroscopic voids in the analyzed granules $A_{void\text{-}e}$ and the sum of all granule areas $A_{total\text{-}e}$, including pores, according to equation (2).

$$H = \frac{\sum_{1}^{n} A_{void-e}}{\sum_{1}^{n} A_{total-e}} \quad (2)$$

An *H* value of 1 % means 1 % of the equatorial granule area is represented by the void. According to the calculated *H* values for every granule, granules are classified into three classes (homogeneous, intersection and hollow (Table 2)), which are yielded from the respective granule counts (N_{homo}, N_{inter} and N_{hollow}) in the measurement plane and can be calculated using equations (3) to (6).

$$M_{homo} = \frac{\sum_{1}^{n} N_{homo}}{N_{total}} \cdot 100\ \% \quad (3)$$

$$M_{inter} = \frac{\sum_{1}^{n} N_{inter}}{N_{total}} \cdot 100\ \% \quad (4)$$

$$M_{homo} = \frac{\sum_{1}^{n} N_{hollow}}{N_{total}} \cdot 100\ \% \tag{5}$$

$$N_{total} = \sum_{1}^{n} N_{homo} + \sum_{1}^{n} N_{inter} + \sum_{1}^{n} N_{hollow} \tag{6}$$

The primary particles are statistically cut with a cut through the equatorial plane. Thus, the stereological principles are fulfilled for the quantitative characterization of the primary particles, the microporosity and the interparticle spacings. Therefore, the microscopic porosity P_{micro} can be determined using equation (7).

$$P_{micro} = \frac{\sum_{1}^{n} A_{void-mi}}{A_{total-mi}} \cdot 100\ \% = \frac{\sum_{1}^{n} A_{void-mi}}{\sum_{1}^{n} A_{void-mi} + \sum_{1}^{n} A_{solid-mi}} \cdot 100\ \% \tag{7}$$

$$P_{micro} = \frac{\sum_{1}^{n} A_{void-mi}}{A_{total-mi}} \cdot 100\ \% = \frac{\sum_{1}^{n} A_{void-mi}}{\sum_{1}^{n} A_{void-mi} + \sum_{1}^{n} A_{solid-mi}} \cdot 100\ \%$$

From equations (1) and (7), the total porosity P_{total} of the fractionated granule charge can be determined.

$$P_{total} = P_{macro} + \frac{P_{micro} \cdot (100\ \% - P_{macro})}{100\ \%} \quad P_{total} = P_{macro} + \frac{P_{micro} \cdot (100\ \% - P_{macro})}{100\ \%} \tag{8}$$

Identification of gradients in the microstructure was made possible by means of analysis in different areas of the granules (Fig. 7). Hollow granules (Fig. 7a) were investigated in the region of the granule surface ($1.0 \leq r_{granule} \leq 0.90$; labeled "R"), in the middle of the solid shell ($0.8 \leq r_{granule} \leq 0.7$; labeled "¾R") and in the direct region of the inside surface ($0.6 \leq r_{granule} \leq 0.5$; labeled "½R"). For solid granules (Fig. 7b), structural characterization was performed in the region near the granule surface ($1.0 \leq r_{granule} \leq 0.90$; labeled "R"), in the region of half the granule radius ($0.6 \leq r_{granule} \leq 0.5$; labeled "½R") and at the granule center ($0.1 \leq r_{granule} \leq 0$; labeled "0R"). All averages were volume-weighted.

The primary particle size $d_{particle}$ was determined as a further microscopic structural parameter. The characterization parameter for this is the equivalent circle diameter (ECD). This should provide information about any particle migration across the granule cross-section.

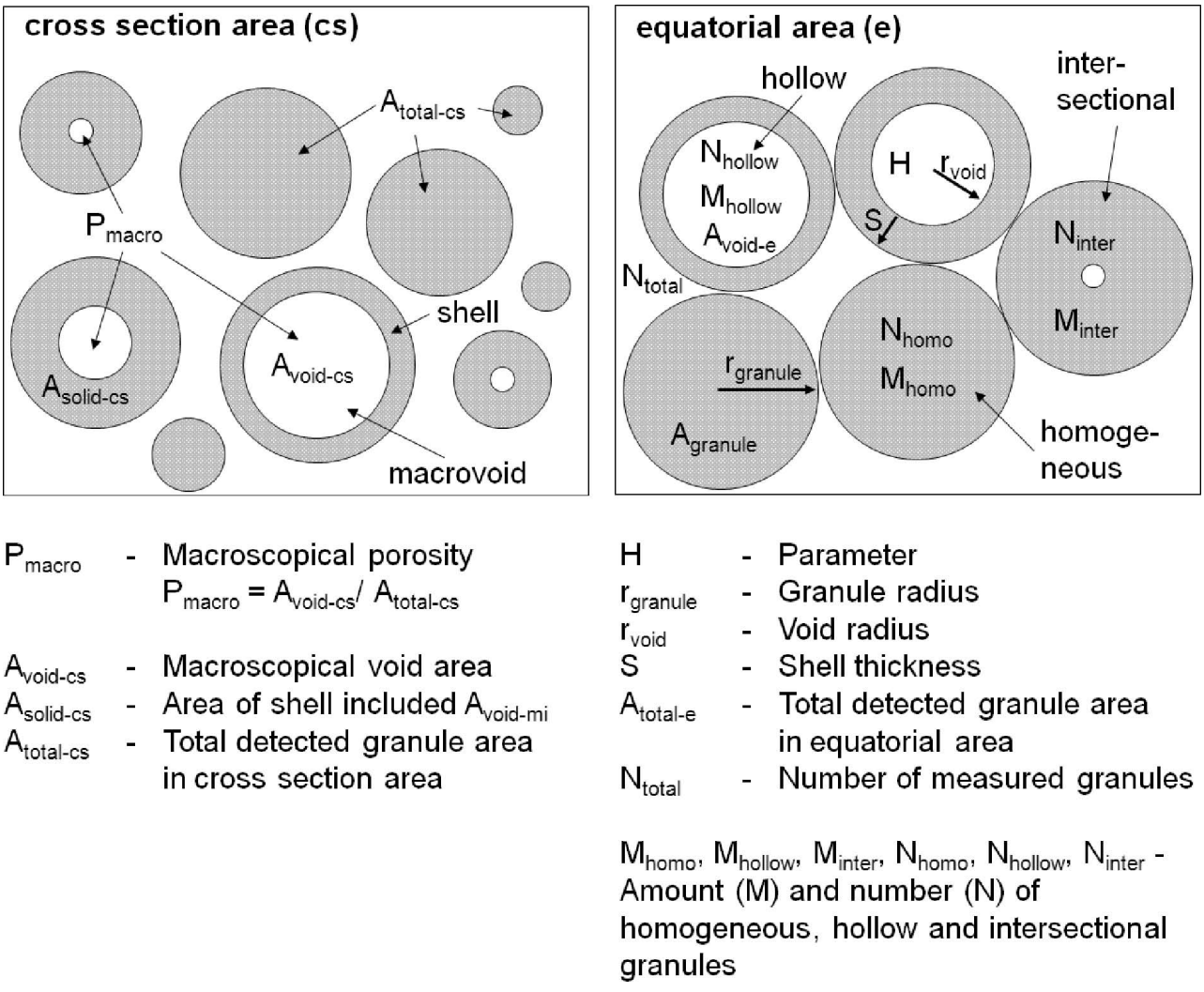

P_{macro} - Macroscopical porosity
$P_{macro} = A_{void-cs} / A_{total-cs}$

$A_{void-cs}$ - Macroscopical void area
$A_{solid-cs}$ - Area of shell included $A_{void-mi}$
$A_{total-cs}$ - Total detected granule area in cross section area

H - Parameter
$r_{granule}$ - Granule radius
r_{void} - Void radius
S - Shell thickness
$A_{total-e}$ - Total detected granule area in equatorial area
N_{total} - Number of measured granules

M_{homo}, M_{hollow}, M_{inter}, N_{homo}, N_{hollow}, N_{inter} - Amount (M) and number (N) of homogeneous, hollow and intersectional granules

Fig. 5: Graphical illustration of defined macroscopic structural parameters in the cross-section and equatorial area.

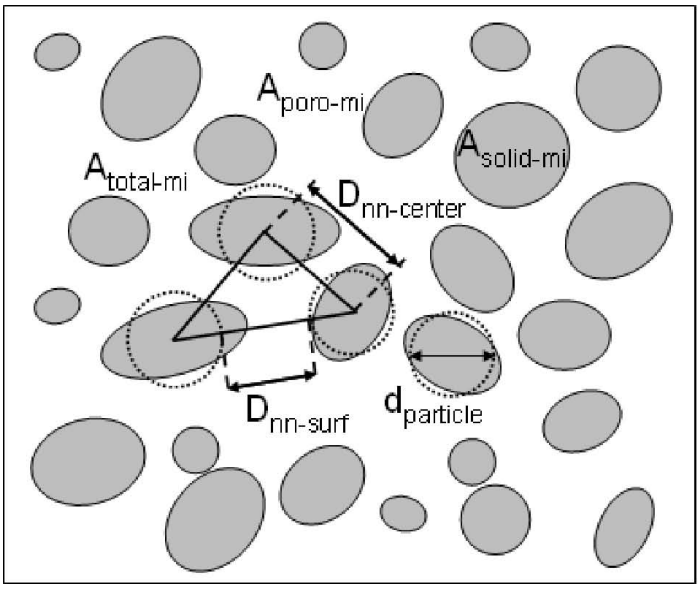

Fig. 6: Graphical illustration of defined microscopic structural parameters.

Because not only the porosity but also the pore size distribution plays a decisive role in the granule properties, a possibility for describing these parameters must be found. One approach is the determination of spatial relationships between the particles via the surface spacing $D_{\text{nn-surf}}$, which can be described in simplified form with equation (9) with the help of the center of gravity spacing D_{center} and the diameters of two particles ($d_{\text{particle-A}}$ and $d_{\text{particle-B}}$).

$$D_{nn-surf} = D_{center} - \left(\frac{d_{particle-A}}{2} + \frac{d_{particle-B}}{2} \right) \quad (9)$$

Because both nearest-neighbor and other spatial relationships must be considered, an algorithm from Voronoi (tessellation) [41] and Delaunay (triangulation) [42] was used as the basis for analysis for precise assignment of next particle neighbors.

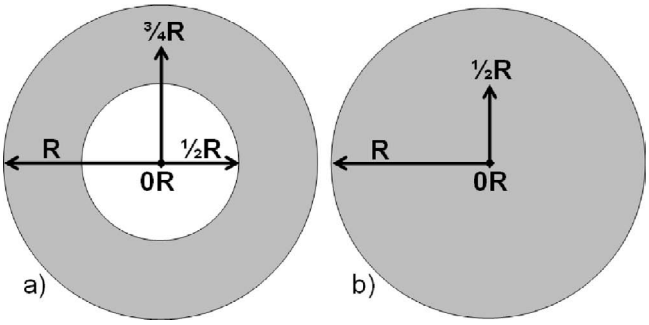

Fig. 7: Analysis areas for microscopic structural parameters for a) hollow granules and b) solid granules.

V. Results and Discussion

(1) Microstructural visualization and EDX analysis

The macroscopic and microscopic structures of granules 1 to 3 are shown in Fig. 8. It is evident from the macroscopic images that granules 1 and 2 are made up of homogeneous and hollow granules and granule 3 primarily of solid granules.

Regarding the microstructure, granule 3 exhibited a considerably looser primary particle structure than granules 1 and 2 did. Visualization of the organic components was not possible for any of the three granules, even at high magnifications. Assumption of a complete and homogeneous wetting of the primary particles with the organic binders ($r_{PVA} \approx 1.3$ g/cm^3) yielded a coating thickness of approx. 1 nm with a specific surface for the starting powder of $S_m = 7.66$ m^2/g and an organic additive content in the granule of 1 wt%. Hence, it is clear that SEM imaging of the binder is only possible if it is inhomogeneous, for example, as a shell structure at the outer surface, in junctions, or as islands. With EDX carbon line analysis, the binder could be detected. Using the example of granule 3, Fig. 9 shows an increased binder concentration at the outer granule surface.

To facilitate visualization of the organic additives, granules with increased organic concentrations were prepared. The internal structure of granule 4 is shown in Fig. 10. It can be seen that the zinc stearate used here was distributed homogeneously in the granules but was present as particles or agglomerates and exhibited a flake-like structure. SEM imaging of the binder system in the granule was successful for granule 5. In Fig. 11, it can be seen that the acrylate used was inhomogeneously distributed. This result was confirmed for several granules of this charge as well as in comparative FIB investigations (Fig. 12).

(2) Thermogravimetric investigations

Heating of the samples occurs during sample preparation with ion beams and can result in evaporation and sublimation. For the purposes of determination of the mass changes in the samples as a function of temperature, thermogravimetric investigations (STA 429, Netzsch-Gerätebau GmbH) under comparable conditions were performed in an argon atmosphere/vacuum ($p_{gas} <$ 3 mbar) at a heating rate of 5 K/min.

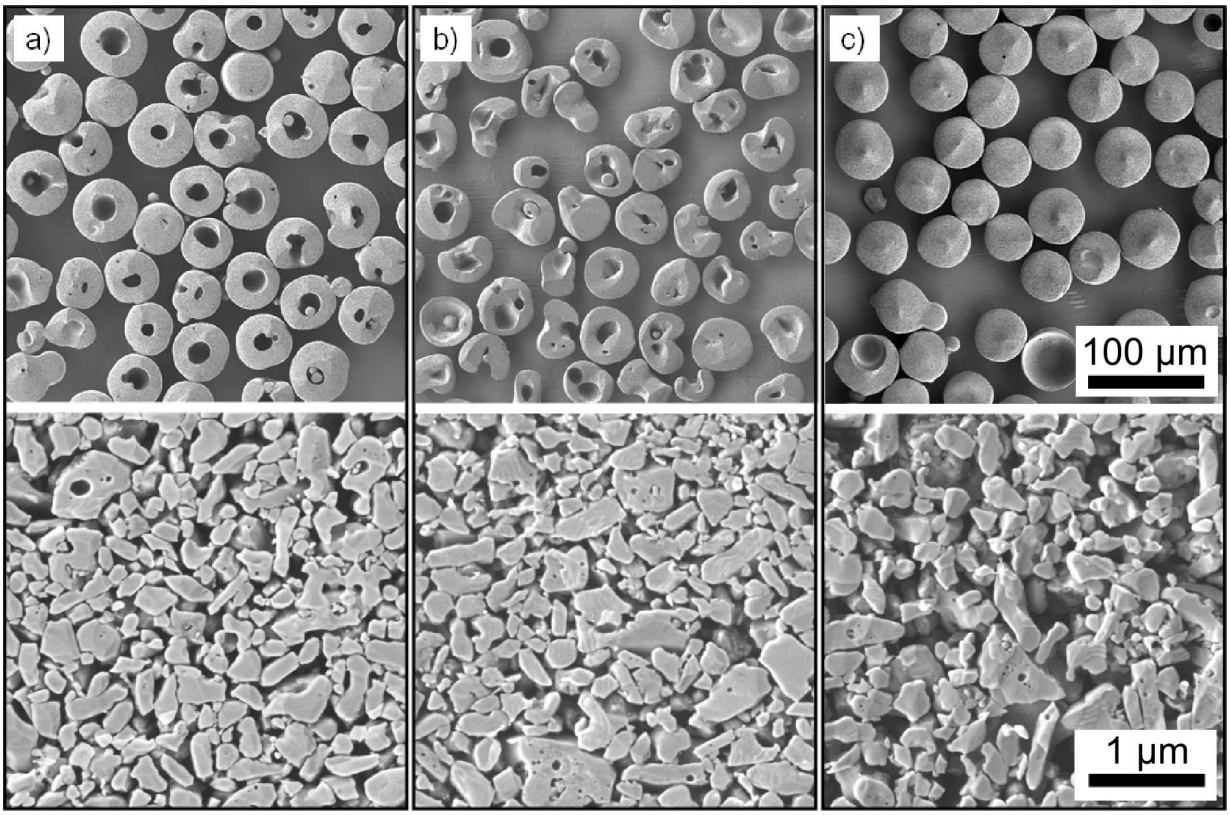

Fig. 8: Granule structures: a) granule 1; b) granule 2; and c) granule 3.

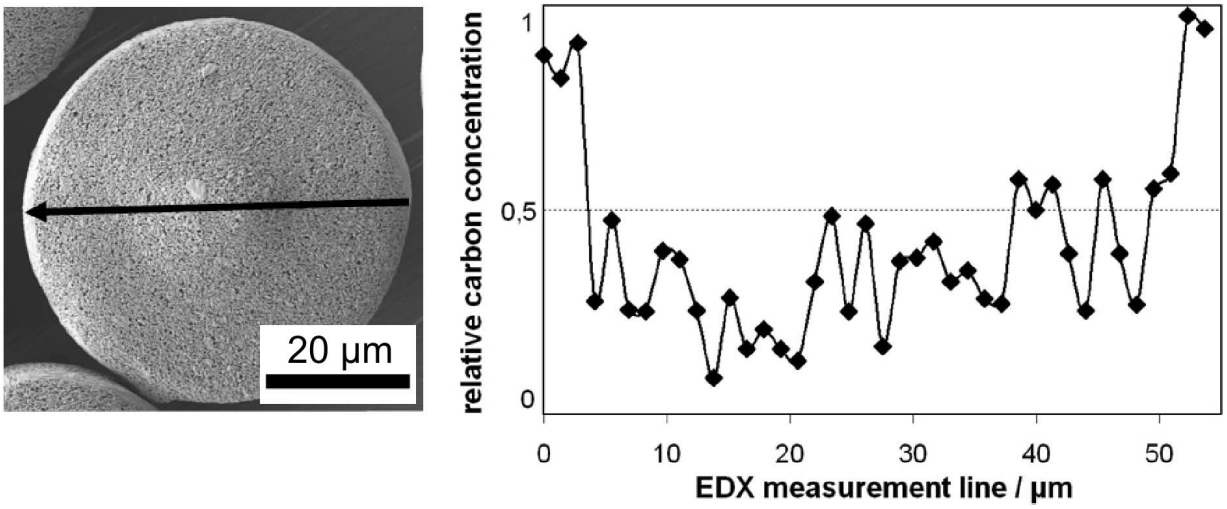

Fig. 9: EDX line analysis using the example of a granule from charge 3.

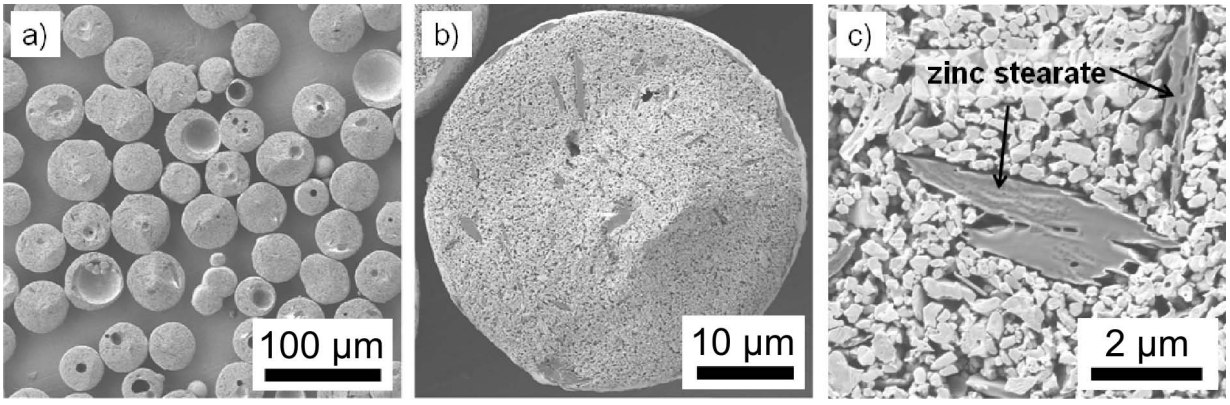

Fig. 10: Structure of granules in charge 4: a) and b) image of overall structure; and c) detailed image.

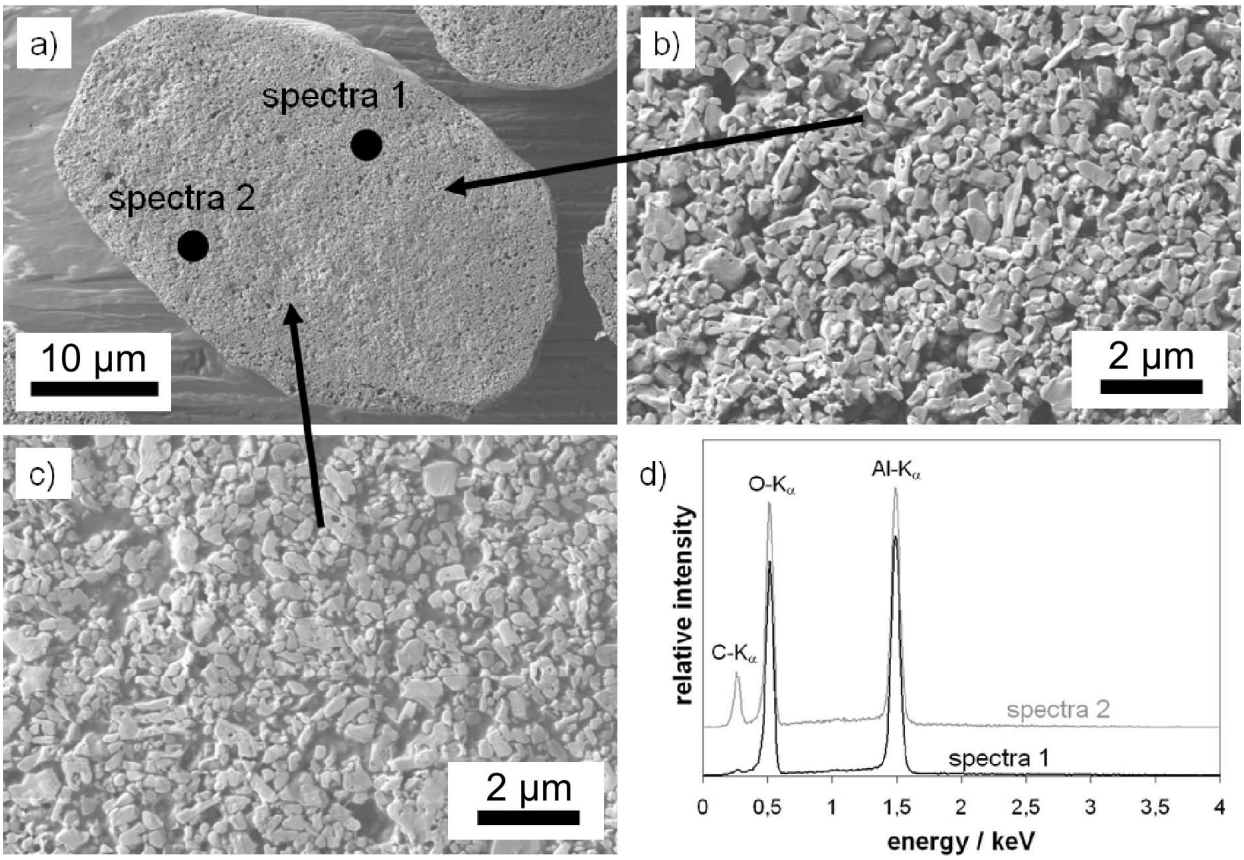

Fig. 11 : Structure of granules in charge 5: a) image of overall structure; b) area with low PVA concentration; c) area with high PVA concentration; and d) EDX point analysis at marked locations.

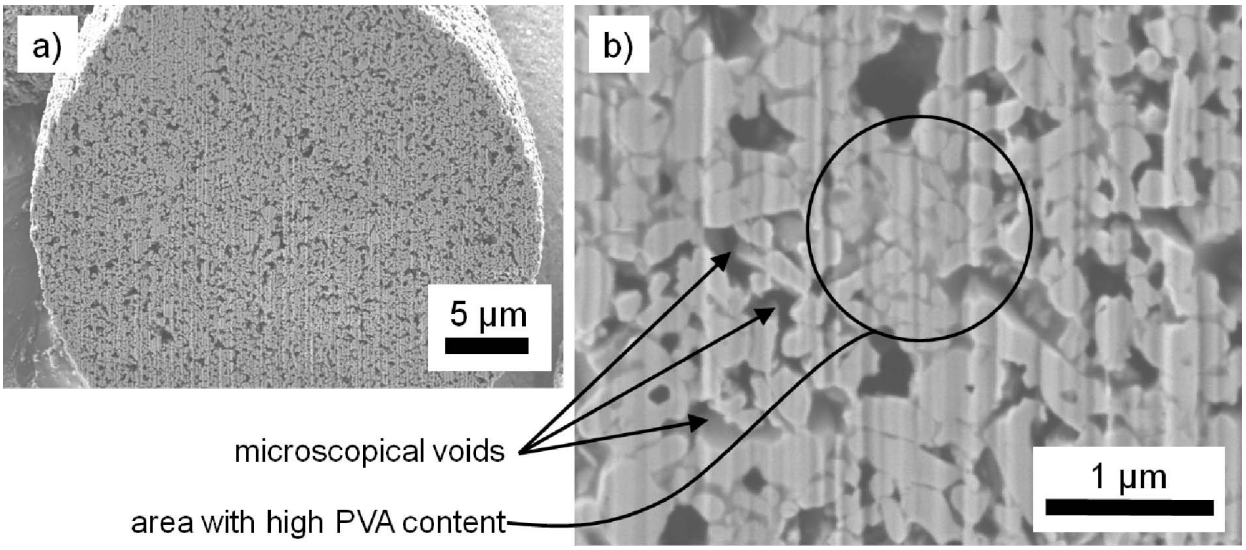

Fig. 12: Results of FIB preparation for a granule from charge 5: a) image of overall structure and b) detailed image.

As can be seen in Fig. 13, a relative mass loss of $m_{rel} \leq 0.1$ wt% up to a temperature of 100 °C and a relative mass loss of $m_{rel} \leq 0.2$ wt% at 150 °C were found for all granule charges. The low initial mass loss for granule charge 4 can be accounted for by a smaller zinc stearate surface area owing to inclusion in the granules in the form of clusters or possibly to different kinetics of heating. It can be concluded from this that the ion beam preparation regime must be controlled in such a manner that during the preparation process a maximum temperature of approx. 100 °C is not exceeded. These boundary conditions can be ensured by adaptation of the removal rate, introduction of preparation pauses and cooling of the sample holder during preparation, among other things.

(3) Quantitative macrostructural analysis

The results of the macrostructural quantification of granules 1 to 3 are presented in Table 3 below.

Table 3: Classification of granules 1-3 and quantification of macrostructural parameters P_{macro} and S.

	M_{hollow} [%]	M_{inter} [%]	M_{homo} [%]	P_{macro} [%]	S [µm]
Granule 1	36.5 ± 0.3	27.9 ± 0.3	35.6 ± 0.3	2.2 ± 0.1	19.5 ± 0.2
Granule 2	39.1 ± 0.3	27.0 ± 0.3	33.9 ± 0.3	3.1 ± 0.1	18.5 ± 0.2
Granule 3	4.8 ± 0.3	12.3 ± 0.3	82.9 ± 0.3	0.2 ± 0.1	23.5 ± 0.3

It can be seen that the subjective impression that the granules in the investigated granule charge 3 are more homogeneous can be proven with these results. At 82.9 %, the amount of homogeneous granules for sample 3 is much higher than for samples 1 and 2. The low amount of homogenous granules in granule 1 and 2 is accompanied by lower calculated average shell thicknesses. These calculated average shell thicknesses *S* of the granules can be a starting point for correlation between macrostructural parameters and measured mechanical properties of the granules. This is one topic for further research work.

The results presented are based on the assumption that the granules are cut in the middle, i.e. exactly along the equatorial plane. If the cut deviates by the value *y*, there is a relative error for porosity s_{rel}, which can be mathematically described by equation (10).

$$s_{rel} = 100\% - \frac{100\%\left(1-\frac{y^2}{r_{void}^2}\right)}{1-\frac{y^2}{r_{granule}^2}} \qquad \forall\ y \geq r_{void},\ s_{rel} = 100\% \tag{10}$$

Fig. 14 illustrates how high s_{rel} becomes when the granules are analyzed at planes other than the equatorial plane. It can be seen that for granules with small macropores, the granules must be cut precisely in the middle.

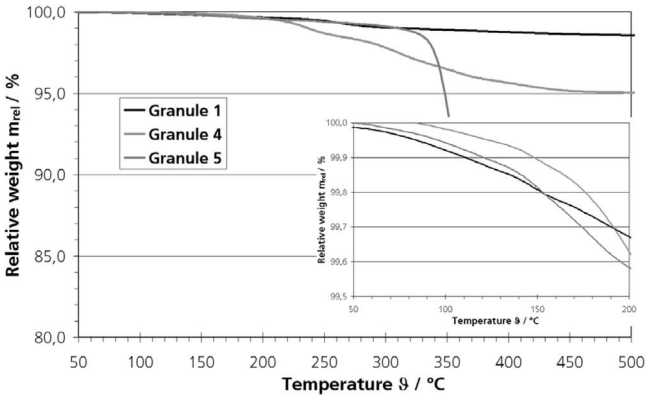

Fig. 13: Results of thermogravimetric analysis for granule charges 1, 4 and 5.

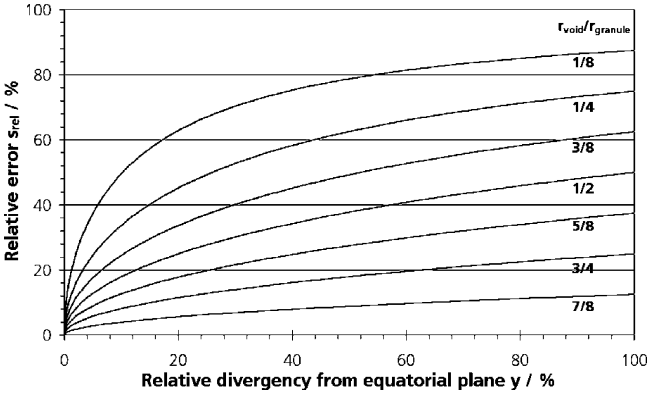

Fig. 14: Visualization of relative error for porosity for granule cut for various divergences from equatorial plane.

(4) Quantitative microstructural analysis

Table 4 summarizes the results of microstructural analysis of granules 1 to 3.

Table 4: Quantification of P_{micro}, $D_{nn\text{-}sur}$ and $d_{particle}$ of granules 1-3.

	Classification	Parameter	Analysis Area				
			OR	½R	¾R	R	Ø
Granule 1	Homogeneous	P_{micro} [%]	30.6 ± 0.4	30.7 ± 0.4	-	30.5 ± 0.4	30.6 ± 0.4
		$D_{nn\text{-}sur}$ [nm]	80 ± 2	78 ± 2	-	79 ± 2	79 ± 2
		$d_{particle}$ [nm]	165 ± 5	162 ± 5	-	178 ± 5	172 ± 5
	Hollow	P_{micro} [%]	-	37.6 ± 0.5	34.6 ± 0.4	34.8 ± 0.4	35.3 ± 0.4
		$D_{nn\text{-}sur}$ [nm]	-	96 ± 3	86 ± 3	90 ± 3	90 ± 3
		$d_{particle}$ [nm]	-	169 ± 5	176 ± 5	149 ± 4	162 ± 5
Granule 2	Homogeneous	P_{micro} [%]	37.2 ± 0.4	34.9 ± 0.4	-	31.5 ± 0.4	32.9 ± 0.4
		$D_{nn\text{-}sur}$ [nm]	96 ± 3	87 ± 3	-	79 ± 2	82 ± 3
		$d_{particle}$ [nm]	160 ± 5	163 ± 5	-	180 ± 5	174 ± 5
	Hollow	P_{micro} [%]	-	37.0 ± 0.4	32.4 ± 0.4	34.7 ± 0.4	34.4 ± 0.4
		$D_{nn\text{-}sur}$ [nm]	-	90 ± 3	77 ± 2	83 ± 2	82 ± 2
		$d_{particle}$ [nm]	-	171 ± 5	175 ± 5	167 ± 5	170 ± 5
Granule 3	Homogeneous	P_{micro} [%]	44.0 ± 0.5	45.2 ± 0.5	-	44.7 ± 0.5	44.8 ± 0.5
		$D_{nn\text{-}sur}$ [nm]	115 ± 3	118 ± 4	-	114 ± 3	115 ± 3
		$d_{particle}$ [nm]	166 ± 5	166 ± 5	-	172 ± 5	170 ± 5

Granule 3 exhibits an average microporosity of P_{micro} = 44.8 %, the highest of the three analyzed granules. In granule charge 3, a homogeneous internal structure could be detected along the granule cross-section, confirmed by both the P_{micro} value and the values of $D_{nn\text{-}surf}$ and $d_{particle}$. The same result was obtained from analysis of the solid granules from charge 1, with primary particle sizes ($d_{particle}$ = 178 nm) at the surface being larger than 0R ($d_{particle}$ = 165 nm) and ½R ($d_{particle}$ = 162 nm). A different tendency was found for the solid granules from charge 2. The packing density was found to be considerably higher at the granule center (P_{micro} = 31.5 %) than at the granule surface (P_{micro} = 37.2 %). However, the primary particle size was also larger at the surface ($d_{particle}$ = 180 nm) than at the granule center ($d_{particle}$ = 160 nm).

In the case of the hollow granules from charges 1 and 2, a slightly lower density was found in the sample area adjacent to the central macropore than at the outer granule surface. The primary particle sizes for granule 1 at the surface ($d_{particle}$ = 149 nm) were considerably smaller than ¾R ($d_{particle}$ = 176 nm) and ½R ($d_{particle}$ = 169 nm) were. For granule 2, particle migration of small particles to the granule surface was found to be minimal.

The investigations also yielded higher packing densities for solid granules from charges 1 and 2 than for hollow granules. The solid granules from charge 1 had a P_{micro} of 30.6 %, the lowest intergranular porosity of all analyzed samples. The microstructural investigations revealed differences in granule structure, especially between granule charges 1, 2 and 3 in an objective and quantitative way.

(5) Total porosity analysis

In Table 5, the values calculated for total porosity for granule charges 1 to 3 in analyzed size fraction 45 – 63 µm from microstructural qualification are listed. The results for granules 1 and 2 were on the same order of magnitude. Despite having the lowest macroscopic porosity, granule 3 had the highest total porosity. This suggests that P_{micro} has a greater influence on P_{total} than P_{macro} does.

Table 5: Summary of porosity measurements of granules 1-3.

	P_{macro} [%]	P_{micro} [%]	P_{total} [%]	P_{Hg} [%]
Granule 1	2.2 ± 0.1	33.0 ± 0.4	34.5 ± 0.4	35.8 ± 0.5
Granule 2	3.1 ± 0.1	33.7 ± 0.4	35.8 ± 0.4	36.7 ± 0.5
Granule 3	0.2 ± 0.1	44.8 ± 0.5	44.9 ± 0.5	43.0 ± 0.6

Comparison of the values for P_{total} with the porosity values from mercury porosimetry measurements (P_{Hg}) revealed only slight deviations from the porosities obtained from image analysis. Thus, the results could be confirmed with a second analysis method. The differences could be attributed to the fact that exact separation between individual granule porosity and porosity of the bulk by mercury porosimetry is very difficult, as shown in Fig. 15 for granules 1 and 3. Determination of macroscopic structural parameters by high-resolution CT at resolutions of < 1 µm in the future should yield better results.

As a result of the investigations three defined different granule structures were characterized. Granule charge 1 was observed as round granule with dense packed shells and high number of homogeneous granules. Granule 2 like granule 1 consists of a combination of homogeneous and hollow granules whereas granule 3 showed a high number of homogeneous granules and a loose-packed microstructure. With the developed characterization method these subjective impressions could be quantified – for granule charge 3 the highest amount of homogeneous granules (macrostructure) and highest primary particle distances in combination with highest microporosity (microstructure) could be measured. In contrast to this, for granule charge 1 a much higher amount of hollow granules (macrostructure) in combination with lower primary particle distance and porosity (microstructure) could be detected.

All investigations on the model specimens were performed on a d_{50}-like granule fraction of 45 – 63 µm. In the future it should be determined if the results gained are confirmed for all fractions or if there are dependences regarding granule size and structure.

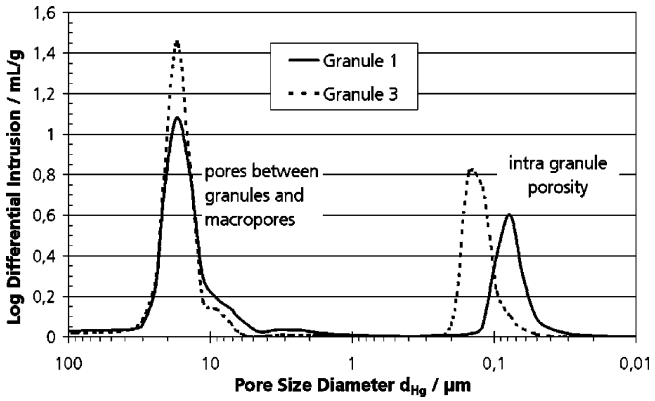

Fig. 15 : Hg porosimetry curves for granule charges 1 and 3.

VI. Summary

In this paper, an ion-beam-based preparation method for highly porous ceramic granules was presented and tested on five model Al_2O_3 granules. This enabled internal granule structures to be prepared reproducibly and gently as a prerequisite for image-analysis-based quantification. It was shown that, apart from high-resolution SEM visualization and quantification of particle and pore structures (samples 1-3), imaging of the additives and their local distributions in the granule cross-sections (samples 4, 5) is possible.

Analysis of macroscopic and microscopic structural parameters was performed on granule charges 1-3. Granule classification, shell thickness analysis and macropore analysis could be performed and shows quantitative differences between the investigated samples. Localized analysis of microstructural parameters such as primary particle size, interparticle porosity and particle spacings enabled structural gradients along the cross-section for granule charges 1 and 2 as well as a homogeneous structure for charge 3 to be identified. Comparisons with established

techniques such as mercury porosimetry yielded results that were in agreement in terms of total porosity.

Key structural parameters are the microscopic porosity P_{micro} and the macroscopic porosity P_{macro}, from which the total granule porosity P_{total} is calculated. Results obtained with the technique for determination of direct spatial relationships between primary particles correlated with the porosity values. In addition, classification into granule types and hollow granule shell thickness represent decisive criteria for granule characterization and future correlation between granule structure and mechanical characteristics. Determination of primary particle distributions in various regions in the granule cross-section delivers information on possible particle migration during the spray granulation process.

Additionally, granule charge 4 was used to demonstrate that the zinc stearate was distributed in the granule cross-sections in flake form. Granule charge 3 exhibited a higher additive concentration at the surface and granule charge 5 was shown to have a very inhomogeneous additive distribution in the granules.

With the methods for quantitative structural characterization of granules described in this paper, new possibilities for analyzing and describing the effects of particle and suspension properties as well as process conditions during spray drying on the resultant granule structure in greater detail were compiled. The new methodological building blocks yield improved possibilities for the optimization of the granule preparation and processing steps and the specific adjustment of green bodies and part properties.

Acknowledgments

The German Research Association (DFG) is gratefully acknowledged for funding of this project under framework program 1423 ("Process Spray").

References

1 Salmang, H., Scholze, H.: Ceramics (in German), *Springer Verlag*, Berlin-Heidelberg, (2007).

2 Soottitantawat, A., Peigney, J., Uekaji, Y, Yoshii, H., Furuta, T., Ohgawara, M., Linko, P.: Structural analysis of spray-dried powders by confocal laser scanning microscopy, *Asia-Pac. J. Chem. Eng.*, **2**, [1], 41-46, (2007).

3 Walton, D.E., Mumford, C.J.: Spray dried products – Characterization of particle morphology, *Chem. Eng. Res. and Design*, **77**, [1], 21-38, (1999).

4 Masters, K.: Spray Drying in Practice, SprayDryConsult International ApS, Charlottenlund, (2002).

5 Walker, W.J., Reed, J.S., Verma, S.K.: Influence of slurry parameters on the characteristics of spray-dried granules, *J. Am. Ceram. Soc.*, **82**, [7], 1711-1719, (1999).

6 Fries, M.: Product design of ceramic spray granulates for uniaxial press compaction to large-size components (in German), Doctorial Dissertation, Techn. Univ. Bergakademie Freiberg, (2008).

7 Hotta, T., Nakahira, K., Naito M., Shinohara, N., Okumiya, M., Uematsu, K.: Origin of the strength change of silicon nitride ceramics with the alteration of spray drying conditions. *J. Eur. Ceram. Soc.*, **21**, [5], 603-610, (2001).

8 Bertrand, G., Filiatre, C., Mahdjoub, H., Fossy, A., Coddet, C.: Influence of slurry characteristics on the morphology of spray-dried alumina powders, *J. Eur. Ceram. Soc.*, **23**, [2], 263-27, (2003).

9 Bertrand, G., Roy, P., Filiatre, C., Coddet, C.: Spray-dried ceramic powders: A quantitative correlation between slurry characteristics and shape of granules, *Chem. Eng. Sci.*, **60**, [1], 95-102, (2005).

10 Lukasiewicz, S.J.: Spray-drying ceramic powders, *J. Am. Ceram. Soc.*, **72**, [4], 617-624, (1989).

11 Abe, H., Naito, M., Hotta, T., Kamiya, H., Uematsu, K.: Pore defects related to slurry character and their relevance to strength distribution in alumina ceramics, *Powd. Techn.*, **134**, [1-2], 58-64, (2003).

12 Tsubaki, J., Yamakawa, H., Mori, T., Mori, H.: Optimization of granules and slurries for press forming, *J. Ceram. Soc. Japan*, **110**, [10], 894-898, (2002).

13 Shinoharaa, N., Okumiyaa, M., Hottab, T., Nakahirab, K., Naitob, M., Uematsu, K.: Variation of the microstructure and fracture strength of cold isostatically pressed alumina ceramics with the alteration of dewaxing procedures, *J. Eur. Ceram. Soc.*, **20**, [7], 843-849, (2000).

14 Yu, Y., Wang, J.: Effect of X-ray irradiation on starch granule structure and physicochemical properties of rice, *Food Res. Intern.*, **40**, 297-303, (2007).

15 Baklouti, S., Chartier, T., Baumard, J.F.: Binder distribution in spray-dried alumina agglomerates, *J. Eur. Ceram. Soc.*, **18**, [14], 2117-2121, (1998).

16 Tanaka, S., Chia-Pin, C., Kato, Z., Uematsu, K.: Effect of internal binder on microstructure in compacts made from granules, *J. Eur. Ceram. Soc.*, **27**, [2-3], 873-877, (2007).

17 Komlev V.S., Barinov, S.M., Giradin, E., Oscarsson, S., Rosengren, A., Rustichelli, F., Orlovskii, V.P.: Porous spherical hydroxyapatite and fluorhydroxyapatite granules: processing and characterization, *Sci. and Techn. of Adv. Mat.*, **4**, [6], 503-508, (2003).

18 Wang, S., Yu, J., Zhu, Q., Yu, J., Jin, F., Granular structure and allomorph position in C-type Chinese yam starch granule revealed by SEM, C CP/MAS NMR and XRD, *Food Hydrocolloids*, **23**, [2], 426-433, (2009).

19 Uematsu, K., Kim, J.-Y., Miyashita, M., Uchida, N., Saito, K.: Direct Observation of Internal Structure in Spray-Dried Alumina Granules, *J. Am. Ceram. Soc.*, **73**, [8], 1555-1557, (1990).

20 Kim, J.-Y., Inoue, M., Kato, Z., Uchida, N., Saito, K., Uematsu, K.: Direct observation of internal structure in spray-dried yttria-doped zirconia granule, *J. Mat. Sci.*, **26**, [8], 2215-2218, (1991).

21 Zhang, Y., Suga, T., Kawasaki, K., Tang, X.X., Uchida, N., Uematsu, K.: Effect of PVA Adsorption on Binder Segregation during Drying, *J. Am. Ceram. Soc.*, **79**, [2], 435-440, (1996).

22 Uematsu, K., Ito, H., Zhang, Y., Uchida, N.: Novel characterization method for the processing ceramics by polarized light microscope with liquid immersion technique, *Cer. Trans., Am. Ceram. Soc.*, **54**, 83-89, (1995).

23 Uematsu, K., Saito, M.: Liquid immersion technique coupled with IR microscopy for direct observation of internal structure of ceramic powder compact – with alumina as an example, *J. Mat. Res.*, **14**, 4463-4465, (1999).

24 Saito, Y., Tanaka, S., Uchida, N., Uematsu, K.: CLSM for Ceramic Green Microstructure, *J. Am. Ceram. Soc. Bull.*, **81**, [1], 35-38, (2002).

25 Appoloni, C.R., Macedo, I., Fernandes, C.P.; Philippi, P.C.: Characterization of porous microstructure by x-ray microtomography, *X-Ray Spectr.*, **31**, [2], 124-127, (2002).

26 Farber, L., Tardos, G., Michaels, J.N.: Application of X-ray Micro-Tomography to Study the Morphology and Porosity of Pharmaceutical Granules, *Microsc. Microanal.*, **8**, [2], 784-785, (2002).

[27] Farber, L., Tardos, G., Michaels, J.N.: Use of X-ray tomography to study the porosity and morphology of granules. *Powd. Techn.*, **132**, [1], 57-63, (2003).

[28] Salvo, L., Cloetens, P., Maire, E., Zabler, S., Blandin, J.J., Buffiere, J.Y., Ludwig, W., Boller, E., Bellet, D., Josserond, C.: X-ray microtomography – an attractive characterisation technique in materials science, *Nucl. Instr. Meth. Phys. Res.*, **B200**, 273-286, (2003).

[29] Rahmanian, N., Ghadiri, M., Jia, X., Stepanek, F.: Characterisation of granule structure and strength made in a high shear granulator, *Powd. Techn.*, **192**, [2], 184-194, (2009).

[30] Herrmann, M., Schulz, I., Bales, A., Sempf, K., Höhn, S.: "Snow flake" structures in silicon nitride ceramics – Reasons for large scale optical inhomogeneities, *J. Eur. Cer. Soc.*, **28**, [5], 1049-1056, (2008).

[31] Baumann, A., Brieseck, M., Höhn, S., Moritz, T., Lenk, R.: Developments in Multi-Component Powder Injection Moulding of Steel-Ceramic Compounds using Green Tapes for In-mould Label Process, *Powd. Inj. Mold. Int.*, **2**, [1], 55-58, (2008).

[32] Mannschatz, A., Höhn, S., Moritz, T.: Powder-binder-separation in injection moulded green parts, *J. Eur. Cer. Soc.*, **30**, [14], 2827-2832, (2010).

[33] Grove, W.R.: LXXIX. On the Electro-Chemical Polarity of Gases. *Phil. Mag.*, **4**, [28], 498-514, (1852).

[34] Plücker, J.: On the influence of magnets on electrical discharges in dilute gases (in German), *Ann. Phys.*, **179**, [1], 88-106, (1858).

[35] Davies, S.T.: Ion beam milling of microelectronic components (in German), *Feinwerkt. u. Messt.*, **95**, 243-244, (1987).

[36] Liebel, G.: Ion beam etching – a reliable method for the production of microstructures (in German), *Feinwerkt. u. Messt.*, **95**, 436-440, (1987).

[37] Seliger, R.L., Ward, J.W., Wang, V., Kubena, R.L.: A high-intensity scanning ion probe with submicrometer spot size, *Appl. Phys. Lett.*, **34**, [5], 310-312, (1979).

[38] Wechsung, R., Aberle, L.: A penning ion source with even beam profile (in German), *Vakuum-Techn.*, **24**, [8], 217-222, (1975).

[39] Barna, A., Szigethy, D.: Ion source for generating ions of a gas or vapour. EP0928495, (1996).

[40] Kaufman, H.R.: Technology of Electron-Bombardment Ion Thrusters, *Adv. Electr. Phys.*, **36**, 265-373, (1974).

[41] Voronoi, G.: New applications of continuous parameters in the theory of quadratic forms (in French), *J. Reine u. Angew. Math.*, **134**, 198-287, (1908)

[42] Delaunay, B.N.: On the Empty Sphere (in French), In: Bull. Acad. Science USSR VII: *Class. Sci. Meth.*, 793-800, (1934).